Tunable Plasmonic Metasurfaces for Optical Phased Arrays

Antonino Calà Lesina, Dominic Goodwill, Eric Bernier, Lora Ramunno, and Pierre Berini

(Invited Paper)

***Abstract*—Controlling the phase and amplitude of light emitted by the elements (*i.e.*, pixels) of an optical phased array is of paramount importance to realizing dynamic beam steering for LIDAR applications. In this paper, we propose a plasmonic pixel composed of a metallic nanoantenna covered by a thin oxide layer, and a conductive oxide, *e.g.*, ITO, for use in a reflectarray metasurface. By considering voltage biasing of the nanoantenna via metallic connectors, and exploiting the carrier refraction effect in the metal-oxide-semiconductor capacitor in the accumulation and depletion regions, our simulations predict control of the reflection coefficient phase over a range $> 330^\circ$ with a nearly constant magnitude. We discuss the physical mechanism underlying the optical response, the effect of the connectors, and propose strategies to maximize the magnitude of the reflection coefficient and to achieve dual-band operation. The suitability of our plasmonic pixel design for beam steering in LIDAR is demonstrated via 3D-FDTD simulations.**

***Index Terms*—Antenna arrays, antenna radiation patterns, beam steering, dipole antennas, metal-insulator structures, MOS capacitors, optical phase shifters, phased arrays, plasmons, reflectarrays.**

I. Introduction

MOST commercial light detection and ranging (LIDAR) scanners are too bulky and slow for applications requiring a high refresh rate, such as self-driving cars and autonomous machines. Optical phased arrays [1] are much smaller and can tremendously improve the scanning speed as they rely on electronic steering rather than mechanical. An optical phased array is composed of phase-tunable light emitters spatially arranged on a plane, where a single emitter is referred to as a pixel. A pixel can be a source of light, such as a LASER, a waveguide, or a LED. However, a pixel can also be a scatterer, such as a nanostructure in a reflectarray or transmittarray metasurface.

Beam steering via optical phased array is achieved by imposing a phase gradient along a certain direction in the array. Extraneous beams, *e.g.*, produced by grating lobes, need to be minimized in LIDAR applications as they can produce false positives during the scanning process. The pitch a of a matrix of pixels (*i.e.*, the spacing between emitters) if too large, can cause grating lobes of similar amplitude as the main lobe. In order to avoid these grating lobes for any steering angle, the pitch should satisfy $a < \lambda/2$, where λ is the wavelength in the material in which the array is immersed. This requirement trades off with the necessity of having a large enough pitch so that pixels do not interact with each other (no near-field coupling), and each can be controlled independently. Furthermore, if the phase of the field emitted by the pixel does not cover a 360° range, or its amplitude is not uniform across the phase range, the phase gradient will contain imperfections. These imperfections can be periodic with a period much greater than the pitch, thus producing lobes obeying a diffraction grating-type equation; we call these "long-period grating lobes".

Among phase-shifting pixels for optical phased arrays, those based on plasmonic resonances can satisfy $a < \lambda/2$. Thus, plasmonic metasurfaces [2]–[5] offer a platform to implement optical phased arrays that completely avoid grating lobes arising from a too large pitch size. Most plasmonic metasurfaces experimentally demonstrated to date are passive; this means that once fabricated, they cannot be further tuned resulting in a static optical response. Such passive metasurfaces have been proposed for focusing [6], achromatic lensing [7], perfect absorption [8], colouring [9], performing mathematical operations [10], holography [11], nonlinear field enhancement [12], beam structuring in the linear [13] and nonlinear [14] regimes, and biosensing [15]. However, there is a growing interest in active plasmonics to control the field emitted by individual nanostructures by tuning their surface plasmon resonances [16], and in tunable metasurfaces with reconfigurable optical response [17], [18] for applications in dynamic holography and optical information encryption [19], adaptive beamforming in wireless communications [20], chirality switching [21], active displays [22], polarization conversion [23], metalenses with tunable focus [24], dynamic beam steering [25], [26], and intensity modulators [27].

Manuscript received January 15, 2020; revised March 20, 2020 and April 13, 2020; accepted April 22, 2020. Date of publication April 29, 2020; date of current version June 16, 2020. *(Corresponding author: Antonino Calà Lesina.)*

Antonino Calà Lesina and Pierre Berini are with the Department of Physics and the Centre for Research in Photonics, University of Ottawa, Ottawa, ON K1N 6N5, Canada, and also with the School of Electrical Engineering and Computer Science, University of Ottawa, Ottawa, ON K1N 6N5, Canada (e-mail: antonino.calalesina@uottawa.ca; berini@eecs.uottawa.ca).

Dominic Goodwill and Eric Bernier are with the Huawei Technologies Canada, Kanata, ON K2K 3J1, Canada (e-mail: dominic.goodwill@huawei.com; eric.bernier@huawei.com).

Lora Ramunno is with the Department of Physics and the Centre for Research in Photonics, University of Ottawa, Ottawa, ON K1N 6N5, Canada (e-mail: lora.ramunno@uottawa.ca).

This article has supplementary downloadable material available at https://ieeexplore.ieee.org, provided by the authors.

Color versions of one or more of the figures in this article are available online at https://ieeexplore.ieee.org.

Digital Object Identifier 10.1109/JSTQE.2020.2991386

A pixel controllable in phase can be achieved by exploiting, for example, phase-change materials [28], liquid crystals [29], Fermi-level gating in graphene [30], carrier refraction in semiconductors and transparent conductive oxides (TCOs) including indium-tin oxide (ITO) [31], [32], and the thermo-optic effect in bulk dielectrics [33]. Phase control has also been demonstrated in arrays of coherently-coupled vertical-cavity surface-emitting lasers [34], and via voltage-tunable inter-subband transitions in semiconductor heterostructures exploiting the quantum-confined Stark effect [35].

Tuning the response of plasmonic nanostructures by exploiting the carrier refraction effect in ITO is promising because of the large change in refractive index available in this material (of the order of unity) [36], [37]. Recent experimental [31], [32] and theoretical [26], [38] studies of phase control for beam steering and focusing, using metallic or dielectric resonant systems, are encouraging. In [31], [32], [38], out-of-plane field enhancement was exploited in metal-insulator-metal (MIM) nano-resonators, where oxide and ITO were placed between the two metal layers. In these cases, the carrier density variation was induced in ITO via single [31] or double [32] gating. The bottom layer was a plane metallic surface, whereas the other layer was either a linear [31], [38] or fishbone [32] grating. The phase range achieved in MIM configurations was $< 300^{\circ}$[26], [38] for single gating. To achieve a phase range $> 300^{\circ}$ a dual-gated solution was proposed [32].

We propose a nanostructure with in-plane resonances as a pixel. Our pixel is composed of a metal dipole nano-antenna covered by an insulator, ITO, and a backplane metal mirror. We exploit perturbations in the permittivity of ITO at locations where the nanostructure produces strong field enhancement in the direction of the nanoantenna axis, rather than in the out-of-plane direction as in MIM structures. In our case, fields are strongly enhanced at the extremities of the nanoantenna and within its gap. Exploiting the field enhancement in the gap of a dipole nanoantenna to control the phase of its reflection coefficient has yet to be reported – we show how this plays a major role in achieving reflection with a large tunable phase and an approximately constant magnitude of reflection coefficient, which are fundamental requirements for optical beam steering.

The permittivity of ITO is perturbed via the carrier refraction effect induced in the material, as ITO operates electrically as the semiconductor in a MOS capacitor. In particular, through voltage gating enabled by metallic connectors, we induce a perturbation of the carrier density over a thin ITO region near the nanoantenna via accumulation and depletion processes. In accumulation, the carrier density increases, producing a blue-shift of the epsilon-near-zero wavelength, λ_{ENZ}, of the ITO in this thin perturbed region. As the carrier density increases further, λ_{ENZ} eventually passes through the resonance wavelength of the nanoantenna, and the system transitions from a nanoantenna immersed in a dielectric to a nanoantenna surrounded by a metallic shell. This produces a large red-shift of the nanoantenna resonance wavelength, and as we show in detail, is responsible for the large phase variation observed. We also demonstrate that the phase range can be extended by driving the MOS capacitor into depletion, as depleting the carrier density over an increasing thickness produces an additional sizable phase shift.

Our proposed pixel satisfies the conditions discussed above to minimize grating lobes in optical beam steering, as we will show in Section II via detailed optical and electrostatic simulations. After presenting the numerical approach (Section II-A) and an optimized pixel design via detailed optical simulation (Section II-B), we explain the physical mechanism underlying the large phase shift (Section II-C), and propose a strategy for increasing the amplitude and uniformity of the reflection amplitude (Section II-D). We then explore the effect of the metallic connector position on the resonance of the nanoantenna, and show how this can be exploited to design a dual-band pixel at telecom wavelengths (Section II-E). Our ITO perturbation model is justified via detailed electrostatic simulations (Section II-F). Finally, the use of our proposed pixel for beam steering is demonstrated in Section III via 3D simulations of a reflectarray metasurface using the finite-difference time-domain (FDTD) method.

II. Plasmonic Pixel Design

A. Optical Simulation Approach

1) Description of the Pixel: In Fig. 1(a), we show a sketch of a metasurface that uses, as a building block, our proposed plasmonic pixel illustrated in top-view in Fig. 1(b). The pixel has dimensions a_x by a_z, and contains a gold dipole nanoantenna, which is formed by two branches of length L_d, width w, thickness t, separated by a gap of size g. The pixel also contains two gold lines of width w_c, perpendicular to the dipole, which serve as electrical connectors; the distance between the edge of the connector and the edge of the nanoantenna gap is denoted by p_c. Here, the connectors are placed in the centre of the branches, so that $p_c = 0.5 \cdot (L_d - w_c)$, but they can be located at an arbitrary distance p_c from the edge of the nanoantenna gaps.

The nanoantenna of thickness t sits on a glass substrate, and the nanoantenna/glass system is covered conformally by a thin insulator (oxide, *e.g.*, hafnia) layer of thickness t_{ox}, which is then covered by ITO; see the side view of the pixel illustrated in Fig. 1(c). We denote the thickness of the metasurface (metal nanostructure+oxide+ITO) as t_m. A gold backplane is placed on top of the ITO allowing us to use the pixel in reflection through the glass substrate, and acting as an Ohmic contact to ITO. The backplane is depicted here as a flat layer on planarized ITO but it could also be conformal. The electrically-contacted nanoantennas form the metallization of the MOS capacitor and the gold backplane its ground (Ohmic), with the oxide and ITO forming the insulator and semiconductor regions, respectively. In Fig. 1(b) and (c), we also indicate by the red dotted line the thin ITO layer of thickness t_{pert}, whose refractive index is perturbed by the carrier refraction effect in the MOS capacitor. All corners in our optical computations are square for ease of simulation.

Fabrication of the structure as sketched can be done using standard nanofabrication tools. The gold nanoantenna and connectors can be defined via electron beam lithography and lift-off [39]. The small gaps can be machined via helium (He) focused ion beam (HeFIB) milling [40]. The conformal thin insulator layer can be created via atomic layer deposition (ALD) [41]. The ITO layer that fills all the gaps can be deposited

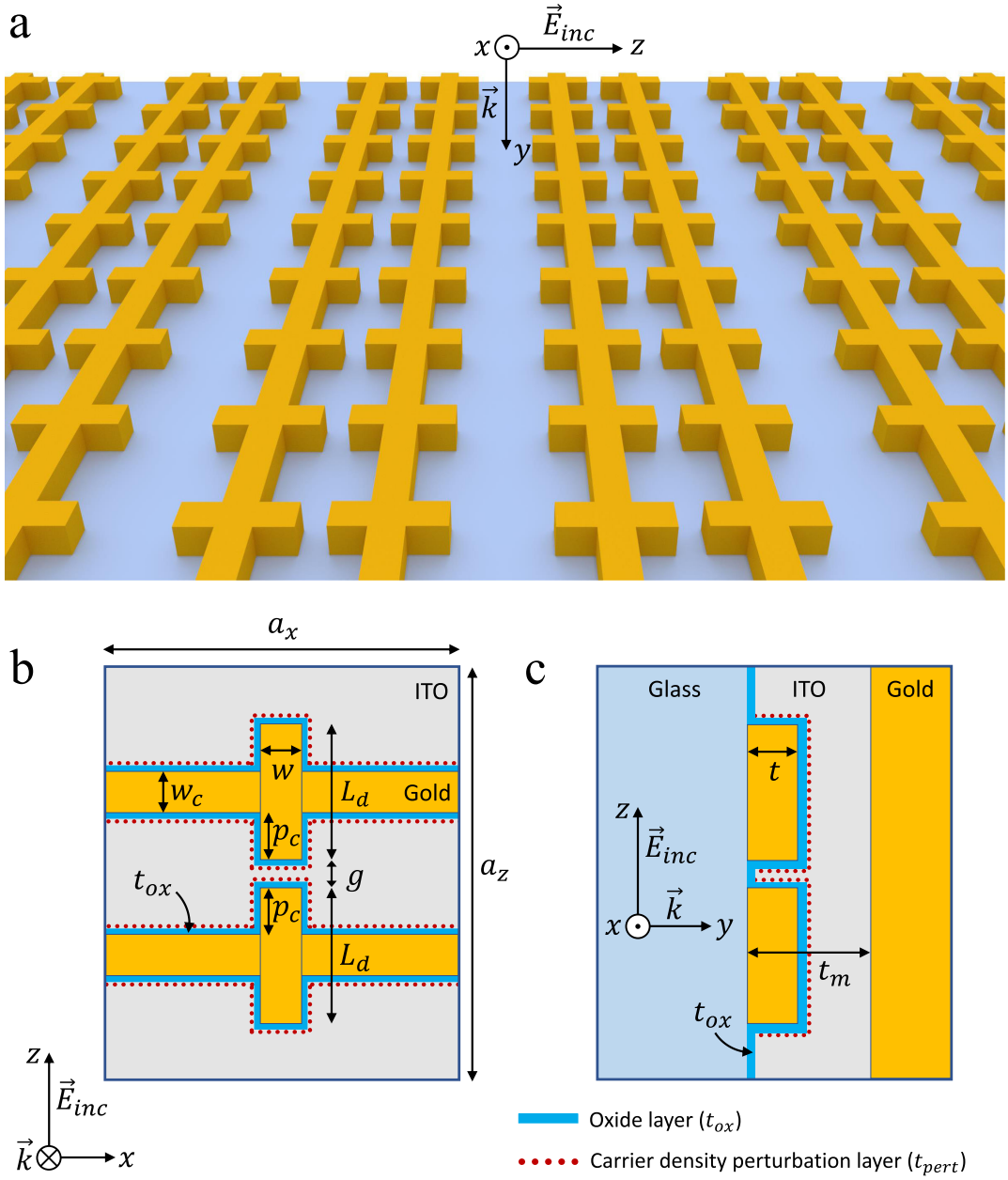

Fig. 1. (a) Metasurface containing an array of plasmonic pixels (only glass substrate and gold nanoantennas are sketched). (b) Top view, and (c) cross-sectional view of the proposed plasmonic pixel. Throughout the paper, the following parameters will remain fixed at their optimized values: $a_z = 500$ nm, $w = 50$ nm, $w_c = 50$ nm, $t = 50$ nm, and $t_{ox} = 5$ nm. The parameters g, L_d, a_x, t_m, and p_c will be varied for optimization.

via sputtering [32], and on top of this layer we can lithographically define the backside metal mirror/Ohmic contact, and pads for contacting to the connectors. As discussed in the next sections, the proposed pixel is sensitive to geometric variations, so large-scale uniformity across the array must be ensured in order to preserve the simulated optical response. Nano-imprint lithography is a viable strategy to replicate nanostructures for mass nanoscale manufacturing [42], as well as state-of-the-art deep ultraviolet lithography [43]. The metasurface (Fig. 1(a)) can be used in a setup where a laser beam hits the surface from the front (incident field $\vec{E}_{inc}$, wavevector $\vec{k}$), and the angle of the reflected beam can be controlled by applying a sequence of voltages to the connectors of the device to steer the beam in the yz-plane. Even though in this study we consider the incoming beam at normal incidence (*i.e.*, $k_x = 0$, $k_y \neq 0$), in an experimental setup we need to make sure that the specular reflection does not hit the laser source. The incident angle plays a negligible role as long as the polarization of the incoming field remains parallel to the axis of the dipole nanoantenna, which can be obtained by tilting the source in the xy-plane (*i.e.*, $k_x \neq 0$, $k_y \neq 0$). Lenses can be used to collimate the beam, then the beam steered in the yz-plane can be used to scan the external environment in, *e.g.*, LIDAR applications.

2) Simulation Details: The optical modelling was conducted with in-house 3D FDTD software [44], [45]. Based on fabrication constraints and optical performance evaluated via detailed

numerical simulations, we found optimal values for a_z, w, w_c, t, and t_{ox} (see the caption of Fig. 1), and they will not be varied throughout this paper. We consider optical (vacuum) wavelengths in the range $\lambda_0 = 1000$ to 1800 nm due to the availability of high-performance, compact and inexpensive laser sources in that range, and all our designs are optimized to operate at telecom wavelengths, *e.g.*, $\lambda_0 = 1550$ nm.

Gold is modelled using the complex permittivity from [46] via the Drude model, *i.e.*, $\varepsilon_r(\omega) = \varepsilon_\infty - \omega_p^2/(\omega^2 + i\gamma\omega)$, where $\varepsilon_\infty = 8.4156$, $\gamma = 4.8257 \cdot 10^{13}$ rad/s, and $\omega_p = 1.4117 \cdot 10^{16}$ rad/s. We choose hafnia (HfO_2) as our insulator, with a layer thickness $t_{ox} = 5$ nm; it is modelled as a lossless and dispersionless dielectric of refractive index $n_{ox} = 2.0709$ (sampled at the operating wavelength) [47]. Glass is simulated as a dispersionless material with $n_{SiO_2} = 1.45$. The permittivity of ITO is modelled via the Drude model with $\varepsilon_\infty = 4.2345$, $\gamma = 1.7588 \cdot 10^{14}$ rad/s, and an ω_p that varies with carrier density N according to $\omega_p = \sqrt{Ne^2/(\varepsilon_0 m_n^*)}$, where e is the electron charge, ε_0 the vacuum permittivity, and $m_n^* = 0.35 \cdot m_e$ the effective mass of electrons; m_e is the free electron mass. The unperturbed carrier density of ITO is taken as $N_0 = 3 \cdot 10^{20}$ cm^{-3}, which corresponds to a plasma frequency $\omega_p = 1.652 \cdot 10^{15}$ rad/s [31], [32].

To optimize the design, we consider an infinite 2D array of the plasmonic pixel, though we simulate only a single unit cell containing one pixel. The unit cell is excited with a z-polarized broadband plane wave pulse propagating along y, and periodic boundary conditions are applied along x and z. We discretize all space dimensions with a uniform space step of 1 nm [45]. We calculate the reflection coefficient $\Gamma(\omega) = E_z(\omega)/E_{inc}(\omega)$, from the known incident field $E_{inc}(\omega)$ and reflected field $E_z(\omega)$; the latter is the only nonzero far-field component due to the z-polarized applied excitation. The reflected field is obtained in the scattered field region at a distance of 600 nm from the nanoantenna, which can be considered far-field for plasmonic systems. At this distance, the reflected field is a plane wave due to the sub-wavelength pixel size and consequent lack of diffraction orders (a_x and $a_z < \lambda/2$, where $\lambda = \lambda_0/n_{SiO_2}$, and λ_0 is the vacuum wavelength). The reflectance is defined as $|\Gamma|^2$ and represents the attenuation factor applicable to the optical power.

3) Carrier Refraction Effect: From the Drude model introduced above, we note that the plasma frequency scales with $\sqrt{N}$: this is the origin of the carrier refraction effect. The carrier density can be varied within a thin layer of ITO by exploiting the operation of a MOS capacitor, where the metal nanoantenna represents the gate (connected to a voltage V_g), ITO is used as the semiconductor (connected to a voltage $V_s = 0$ V or ground), and a thin insulating (oxide) layer is placed in between. We consider both connectors of the pixel pinned to the same potential (symmetric perturbation), but dual-gating can also be exploited. As explored in more detail via electrostatic simulations in Section II-F, when a voltage bias V_g is applied to the gate relative to ground, the carrier density changes within a thin ITO layer due to accumulation ($V_g > V_{fb}$) or depletion ($V_g < V_{fb}$) processes, where V_{fb} is the flat band voltage of our MOS capacitor. This local change in carrier density produces a local change in permittivity due to the carrier refraction effect. Since the ITO layer with perturbed carrier density is located in the enhanced field region near the plasmonic nanostructure, its refractive index variation modifies the resonance condition of the nanoantenna and, therewith, the phase of the reflected field.

Based on the electrostatic analysis of the MOS capacitor in Section II-F, we model the local carrier refraction effect in ITO by introducing in the optical model a thin layer of ITO with thickness $t_{pert} = 1$ nm [26], [32], [38], [48], as shown in Fig. 1(b) and (c). The carrier density within the t_{pert} layer is considered uniform and denoted by N_{pert}. The permittivity of the t_{pert} layer is shown in Fig. 2, and we see that the epsilon near zero wavelength λ_{ENZ} – that is, the wavelength for which $\varepsilon_{Re} = 0$ – blue shifts with increasing N_{pert}. Here N_{pert} is allowed to range between 0 and N_0 in depletion, and N_0 and $13 \cdot 10^{20}$ cm^{-3} in accumulation, for a V_g constrained within the breakdown voltage limits, *i.e.*, $|V_g| < V_{bk} = 3.2$ V. Under negative bias, as we will show in Section II-F, the width of the depletion region increases up to $t_{pert} = 2$ nm for $V_g = -V_{bk}$, and this case is considered in optical simulations as well.

B. Optical Performance of Plasmonic Pixel

Now that we have introduced the concept of our plasmonic pixel and how it operates, we turn to the calculation of the reflection coefficient and how it changes as a function of N_{pert} (and thus, gate voltage) in the perturbed ITO layer. We show in Fig. 3 the results for an optimized pixel (with dimensions as reported in the figure caption). In Fig. 3(a), we plot the absolute value of the reflection coefficient $|\Gamma|$ as a function of λ_0 and N_{pert} (15 simulation entries). The most obvious and remarkable feature of Fig. 3(a) is that there is a wavelength – called the constant amplitude wavelength, λ_c – for which $|\Gamma|$ has approximately the same value for all values of N_{pert} – we call this the constant amplitude point, corresponding to a set of 15 reflection coefficient amplitudes, that are almost coincident. The optimization of the pixel is conducted such that λ_c coincides with the operating wavelength, *i.e.*, $\lambda_c = 1550$ nm (vertical black dashed line). Furthermore, plotting the phase of Γ ($\angle\Gamma$) in Fig. 3(b), we see that at λ_c (vertical black dashed line) there is a large variation with N_{pert}.

Using the relation between V_g and N_{pert} obtained by electrostatic simulations in Section II-F, we plot $|\Gamma|$ and $\angle\Gamma$ in Fig. 3(c) and (d), respectively, as functions of V_g for wavelengths close to λ_c. Here it is evident that at λ_c, $|\Gamma|$ is nearly constant and $\angle\Gamma$ goes through a large variation. These are desirable characteristics for the realization of beam steering at λ_c with long-period grating lobes within an acceptable level. Considering all the 15 simulation entries (highlighted as blue dots in Fig. 3(c)) from Fig. 3(a) at λ_c, we obtain an average reflection coefficient $|\Gamma|_{avg} \sim 0.25$. Not only should $|\Gamma|_{avg}$ be large, but the sequence of blue dots in Fig. 3(c) should also be flat. This means that the percentage standard deviation and the percentage variation of $|\Gamma|$, indicated as $|\Gamma|_{std}$ and $|\Gamma|_{var} = (|\Gamma|_{max} - |\Gamma|_{min})/(|\Gamma|_{max} + |\Gamma|_{min})$, respectively, and reported in Fig. 3(c), have to be as small as possible, ideally zero, in order to reduce the level of the long-period grating lobes of a steered beam.

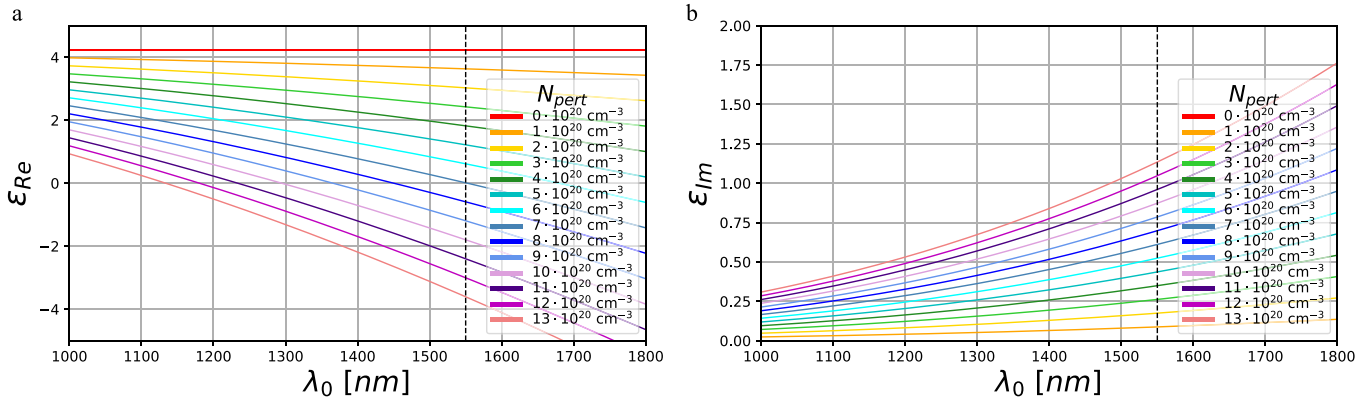

Fig. 2. (a) ε_{Re} and (b) ε_{Im} of ITO *vs.* λ_0 for varying N_{pert}. This permittivity is applied within the perturbed ITO layer of thickness t_{pert} in the optical model.

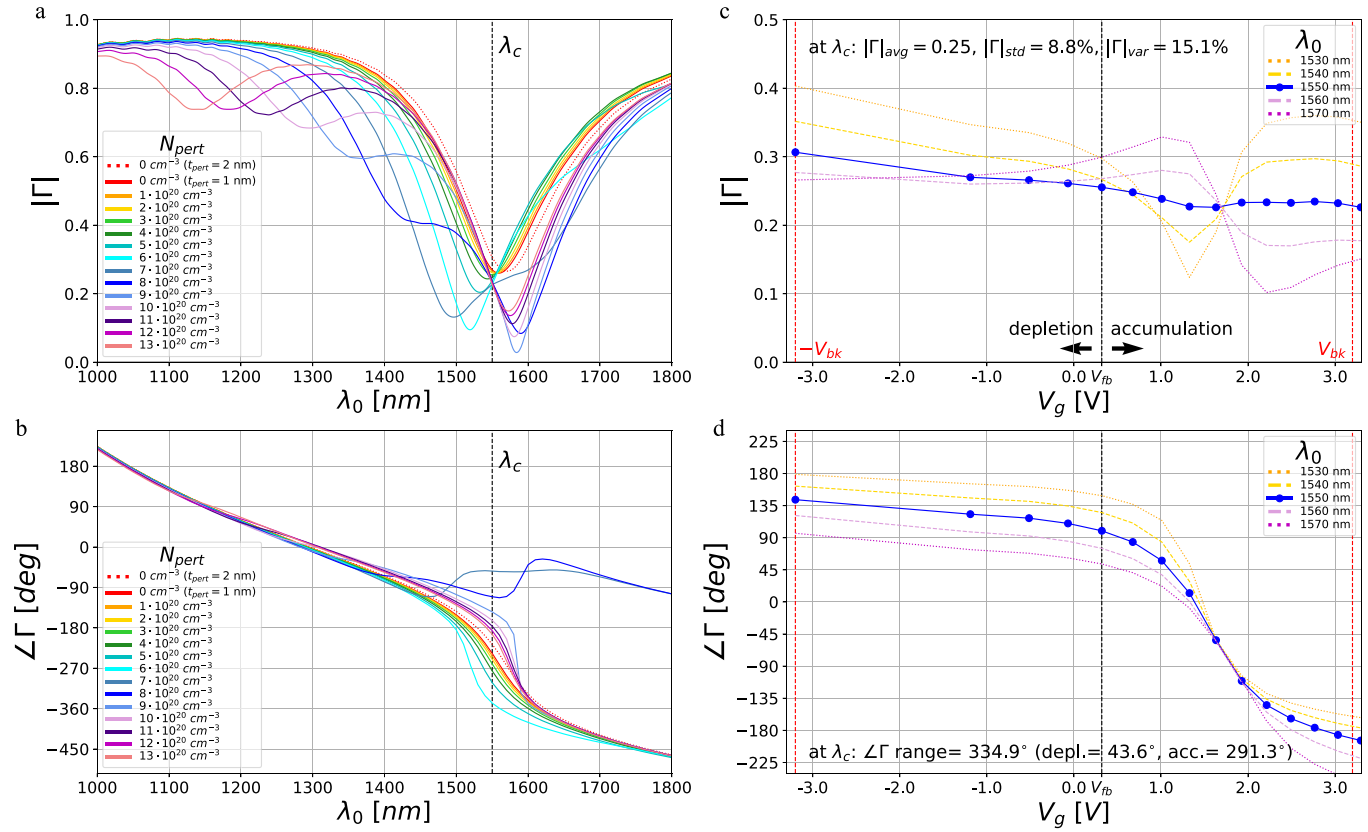

Fig. 3. An optimized pixel with parameters $g = 30$ nm, $L_d = 194$ nm, $a_x = 500$ nm, $t_m = 89$ nm, and $p_c = 0.4 \cdot (L_d - w_c)$: (a) $|\Gamma|$ and (b) $\angle\Gamma$ *vs* λ_0 for varying N_{pert} within the t_{pert} layer. (c) $|\Gamma|$ and (d) $\angle\Gamma$ *vs* V_g for λ_0 near λ_c. The phase plots are unwrapped for clarity.

As reported in Fig. 3(d), the phase range achieved at λ_c within the voltage breakdown limit is $\sim 334°$, where $\sim 291°$ is obtained in accumulation and $\sim 43°$ in depletion. In accumulation, λ_{ENZ} of the perturbed ITO layer passes through λ_c as N_{pert} increases; this is evident in Fig. 3(a), where the $|\Gamma|$ curves show a resonance dip close to λ_{ENZ} which blue-shifts for increasing N_{pert}. This mechanism plays the main role in shifting the phase of the reflection coefficient, as we explain in more detail in Section II-C. As already mentioned, we also consider the case $N_{pert} = 0$ cm^{-3} with $t_{pert} = 2$ nm, which can be reached by the MOS capacitor in depletion at the limit of the oxide breakdown. This simulation condition is reported in Fig. 3(a) as the red dotted curve, and shows a red shift of the response with respect to λ_c. The red shift is due to the larger t_{pert}, and results in an increase in $|\Gamma|$ in Fig. 3(c) as V_g approaches $-V_{bk} = -3.2$ V.

C. *Effect on Phase Shift Due to Changing* λ_{ENZ}

To better understand the operation of our plasmonic pixel and see more clearly how the resonance dips evolve with increasing

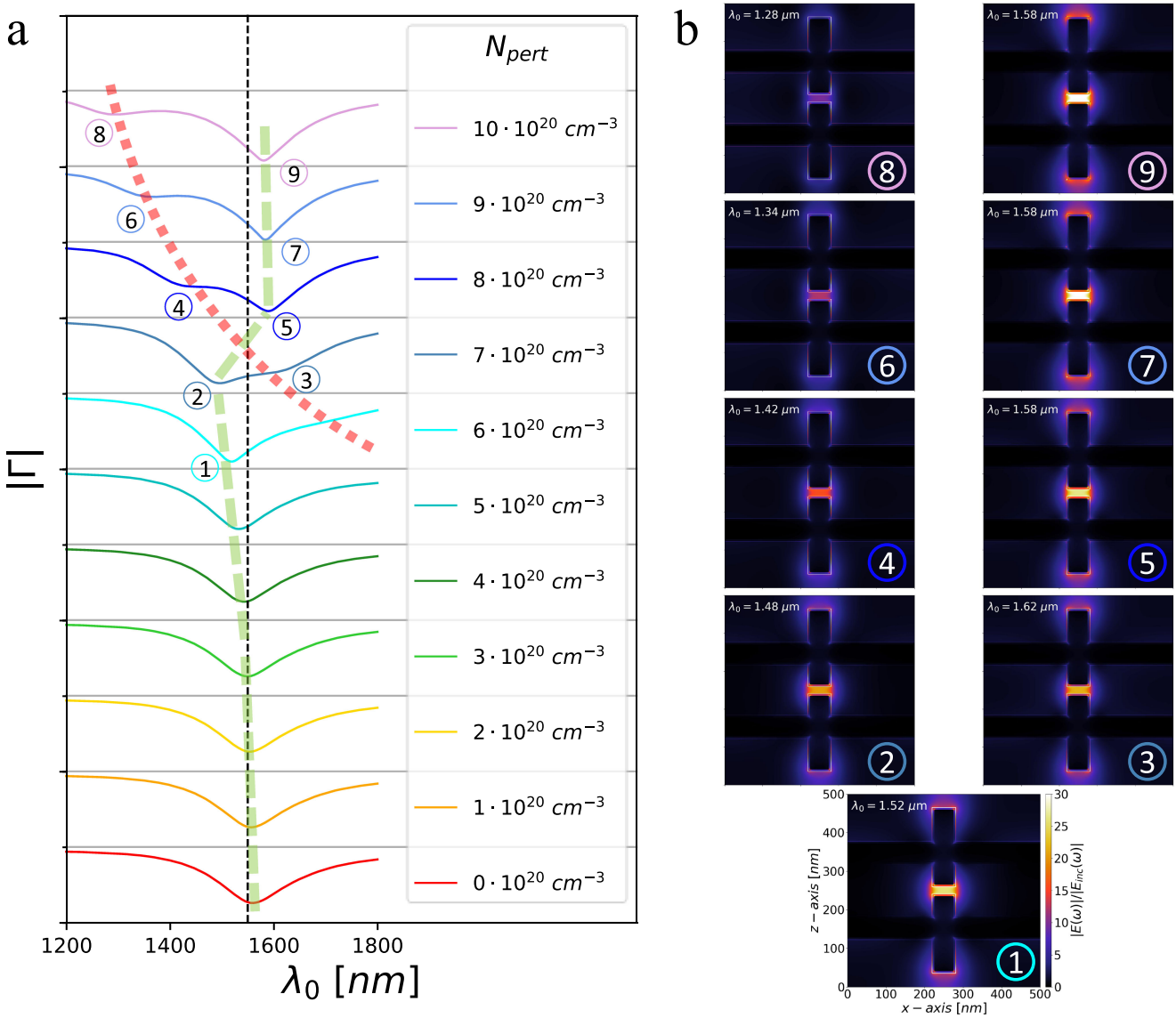

Fig. 4. Response of the optimized pixel of Fig. 3: (a) $|\Gamma|$ *vs.* λ_0 for varying N_{pert} as indicated in the legend. $|\Gamma|$ varies between 0 and 1 for all curves, and this range is marked by the grid lines. (b) Field distribution within the pixel for wavelengths corresponding to the resonances identified by numerals in Fig. 4(a).

N_{pert}, we plot in Fig. 4(a) the spectra from Fig. 3(a), but spread out along the horizontal axis. The operating wavelength $\lambda_c = 1550$ nm is indicated by the vertical black dashed line. As we can see, this wavelength coincides with the resonance dip of the system in the unperturbed case ($N_{pert} = 3 \cdot 10^{20}$ cm^{-3}). The red dotted curve in Fig. 4(a) tracks the value λ_{ENZ} within the perturbed ITO layer as N_{pert} is varied, which we can see is associated with a closely located resonance dip. The green dashed line tracks the evolution of the main nanoantenna resonance dip.

When $\lambda_{ENZ} > \lambda_c$, the perturbed ITO layer around the nanoantenna is dielectric and its refractive index decreases with increasing N_{pert}, producing a blue shift of the main nanoantenna resonance dip (see green dashed line for $N_{pert} \leq 7 \cdot 10^{20}$ cm^{-3}). This suddenly changes when λ_{ENZ} passes through λ_c (see intersection of red dotted curve and black dashed line). For $\lambda_{ENZ} < \lambda_c$, the perturbed ITO layer becomes a metallic sheath, which makes the nanoantenna effectively larger and produces a sudden red-shift of the resonance wavelength (see jump of the green dashed line for $N_{pert} > 7 \cdot 10^{20}$ cm^{-3}).

We need to point out that this phase shift mechanism can only work if λ_{ENZ} for the unperturbed ITO is greater than the resonance wavelength of the nanoantenna. This condition can be satisfied in ITO and other TCO materials, where the free carrier density can be regulated so that λ_{ENZ} is located in the infrared.

In Fig. 4(b), we plot the field distributions associated with the dips labelled by the encircled numerals in Fig. 4(a). We observe the evolution of the resonance mode (tracked by the green dashed line in Fig. 4(a)), and find that it corresponds to a notable field enhancement in the gap of the dipole nanoantenna. This mode evolves following the field distributions labelled by 1-2-5-7-9 in Fig. 4(b) and this series contains the λ_{ENZ} jump across λ_c. The mode associated with the evolution of λ_{ENZ}, indicated by the red dotted curve in Fig. 4(a), follows the field distributions

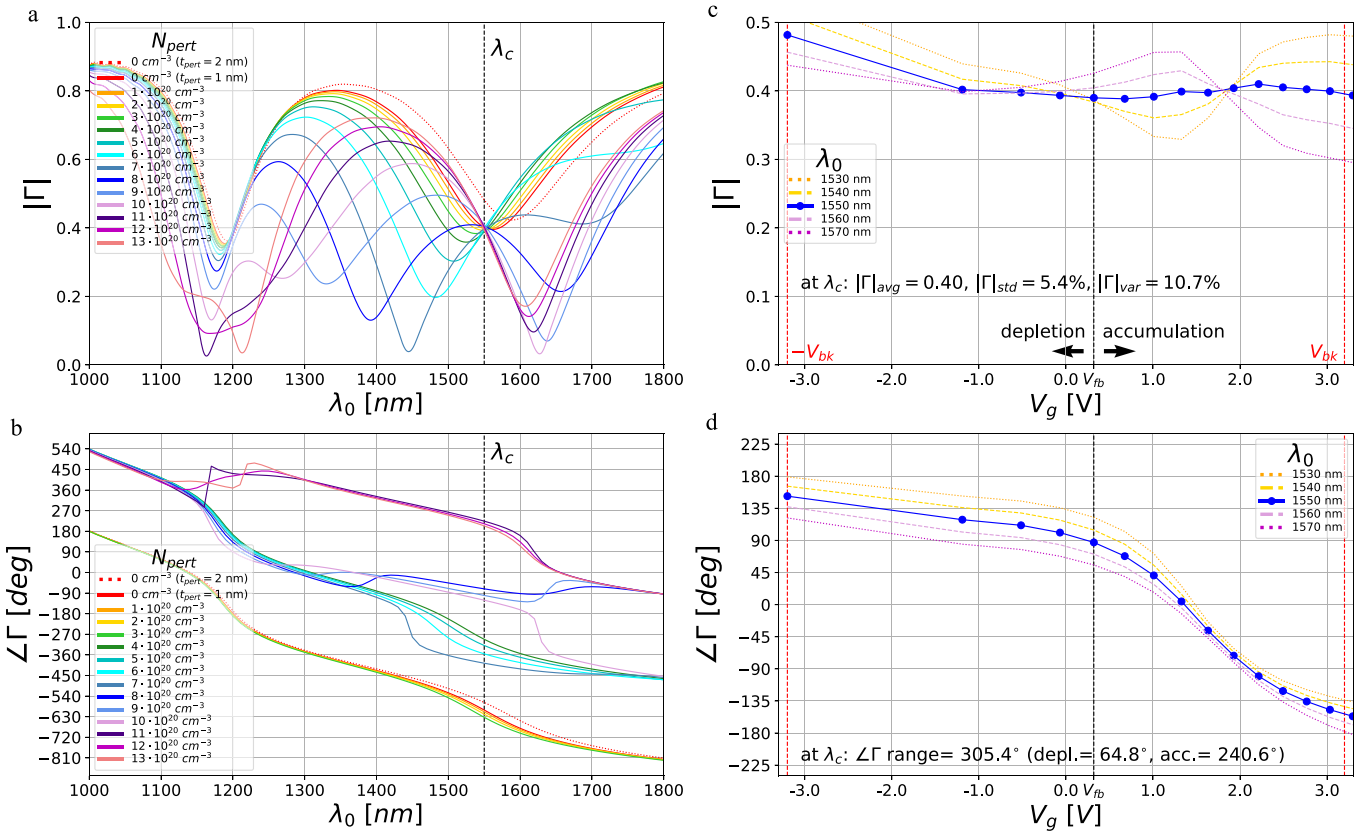

Fig. 5. Second optimized pixel with parameters $g = 15$ nm, $L_d = 149$ nm, $a_x = 298$ nm, $t_m = 100$ nm, and $p_c = 0.5 \cdot (L_d - w_c)$: (a) $|\Gamma|$ and (b) $\angle\Gamma$ *vs* λ_0 for varying N_{pert} within the t_{pert} layer. (c) $|\Gamma|$ and (d) $\angle\Gamma$ *vs* V_g for λ_0 near λ_c. The phase plots are unwrapped for clarity.

labelled by 3-4-6-8 in Fig. 4(b). This mode is characterized by field enhancement in the thin perturbed ITO layer, as is particularly evident in field distributions 4, 6 and 8 of Fig. 4(b). We notice that for $N_{pert} = 7 \cdot 10^{20}$ cm^{-3}, $\lambda_{ENZ} \sim \lambda_c$, the resonance mode of the nanostructure is hybridized, and the field distributions labelled 2 and 3 in Fig. 4(b) are similar.

D. Optimizing the Reflection Coefficient Amplitude and Uniformity

In this subsection we describe strategies for increasing the reflectance at λ_c in the interests of increasing the power efficiency in beam steering applications, and making the reflectance as uniform as possible with varying V_g. To increase pixel reflectance, we increase the field enhancement in the gap of the dipole nanoantenna by reducing the gap length. As the gap must contain two oxide layers, this sets a limit on the smallest possible gap. In Fig. 5, we report the optical simulation results for a second pixel optimized to exhibit a constant amplitude point at λ_c. In this case, the average reflection coefficient at λ_c is 0.4 – two times higher than our previous design above – which yields a $\sim 20\%$ reflectance; the percentage variation is $\sim 11\%$. The phase range in depletion is $\sim 64°$, which is higher than what was reported in Fig. 3 due to the fact that for $t_{pert} = 2$ nm, the gap is almost completely depleted. However, the overall phase range ($\sim 305°$) is lower than that reported in Fig. 3, which suggests that the phase range trades-off against reflectance.

In Fig. 6, we show the optical simulation results for a third pixel optimized to exhibit a constant amplitude point at λ_c. As an appendix to Fig. 6, we show in Supplementary File 1 how the variation of the geometric parameters a_x, t, t_m, and w affects the amplitude of the resonance dips of the $|\Gamma|$ curves (*i.e.*, they move up and down), but with a negligible spectral shift. This affects the intersection of the curves and in turn the uniformity of the reflection coefficient at λ_c. In particular, we observe that decreasing a_x, or increasing t, t_m, or w contribute to the formation of the constant amplitude point in a qualitatively similar way. Furthermore, by comparing Fig. 6 to Fig. 3, we note that in Fig. 6 we have slightly lower $|\Gamma|_{avg}$ and phase range, though $g = 30$ nm in both cases. This suggests that merging the two resonances of the system, as was the case for the optimized design in Fig. 3, may provide a strategy to improve reflectance and phase range. This merging can be achieved by optimizing the connector position, to which we now turn.

E. Effect of the Connector Position and Dual-Band Pixel

We demonstrate in this subsection that the position of the connectors in the pixel significantly alters the optical response. This is an important aspect for the experimental realization of this type of structure. Here we consider only the case where

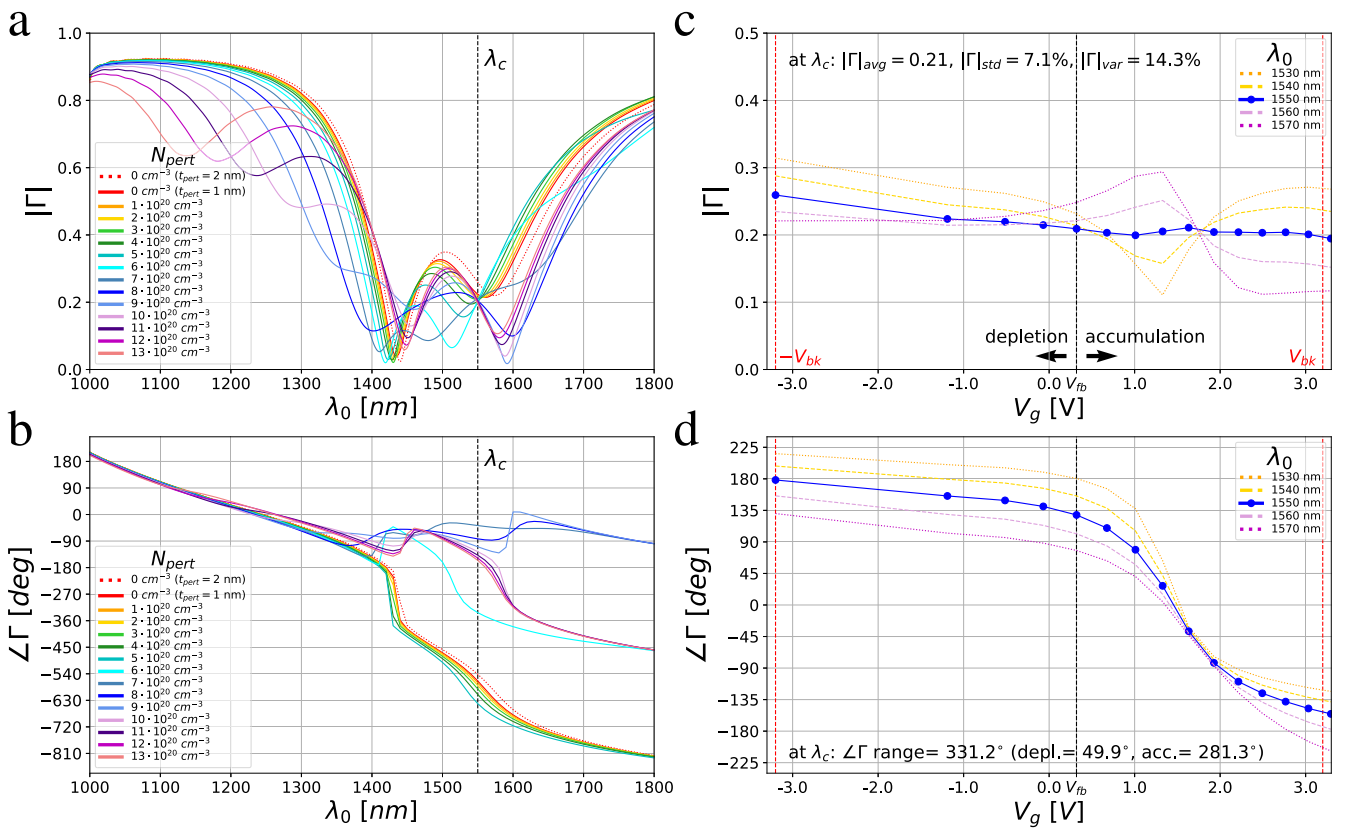

Fig. 6. Third optimized pixel with parameters $g = 30$ nm, $L_d = 186$ nm, $a_x = 404$ nm, $t_m = 100$ nm, and $p_c = 0.5 \cdot (L_d - w_c)$: (a) $|\Gamma|$ and (b) $\angle\Gamma$ *vs* λ_0 for varying N_{pert} within the t_{pert} layer. (c) $|\Gamma|$ and (d) $\angle\Gamma$ *vs* V_g for λ_0 near λ_c. The phase plots are unwrapped for clarity.

the two sets of connectors are equally distant from the gap, *i.e.*, we use the same value of p_c for both branches of the dipole nanoantenna. For the optimized pixel reported in Fig. 3, we used $p_c = 0.4 \cdot (L_d - w_c)$, which results in the plasmonic system exhibiting only one resonance, rendering the connectors optically non-invasive. In the optimized pixels in Section II-D, we used $p_c = 0.5 \cdot (L_d - w_c)$, and this resulted in the reflection coefficient amplitude curves each exhibiting two resonances. Using the parameters of the pixel in Fig. 6 but considering different connector positions, p_c, we will explore the effect of the connector location on the optical response, and the origin of these two resonances.

Considering here unperturbed ITO ($N_{pert} = N_0$), we varied the connector position from $p_c = 0$ to $p_c = L_d - w_c$ to investigate how the resonances evolve with changing p_c. In Fig. 7(a), from bottom to top, we sketch a dipole nanoantenna without connectors, with connectors at position $p_c = 0$ (*i.e.*, located on either size of the gap), with connectors at position $p_c = 0.5 \cdot (L_d - w_c)$ (middle of the branches), and with connectors at position $p_c = L_d - w_c$ (at the extremities of the dipole nanoantenna). In Fig. 7(b), we show the evolution of $|\Gamma|$ as a function of p_c. For some of the resonances in the reflection coefficient, identified by numerals in Fig. 7(b), we plot the corresponding magnitude of the electric near-field in Fig. 7(c). We observe that the single resonance in the case with no connectors splits into two when connectors are introduced: the primary resonance produces field enhancement in the gap of the nanoantenna, whereas the secondary resonance produces field enhancement at the extremities of the branches of the dipole nanoantenna. In the no connector case (field distribution 1, bottom), field enhancement exists in both the gap and the branch extremities. As p_c increases, the two resonances evolve in the spectrum tracing out an "X," *i.e.*, as the primary resonance red-shifts and the secondary resonance blue-shifts (see grey dashed line and grey solid line in Fig. 7(b), respectively). There is a connector position for which the two resonances overlap, which for our example is at $p_c = 0.4 \cdot (L_d - w_c)$ (field distribution identified by numeral 6). This mode strongly resembles the no connector case and identifies the position selected in order for the effect of the connectors on the resonance of the nanoantenna to be minimized. This is the connector position used in our optimized pixel in Fig. 3.

However, the two resonances obtained by introducing the connectors can also be exploited. In Fig. 8, we show results for a fourth optimized pixel that can be used for dual-band beam steering, as it exhibits two constant amplitude wavelengths at the telecom wavelengths $\lambda_c = 1550$ nm and $\lambda_c^{(2)} = 1310$ nm. The phase shifting at both operating wavelengths occurs as λ_{ENZ} transitions through the resonance wavelengths. At λ_c, we have the primary resonance with field enhancement in the gap. In this case, $|\Gamma|_{avg} \sim 0.31$ and the phase range is $\sim 321°$, which follows the trend already observed in Figs. 3 and 5, *i.e.*, reducing the gap size produces a higher magnitude of reflection coefficient and a lower phase range. At $\lambda_c^{(2)}$, we have the

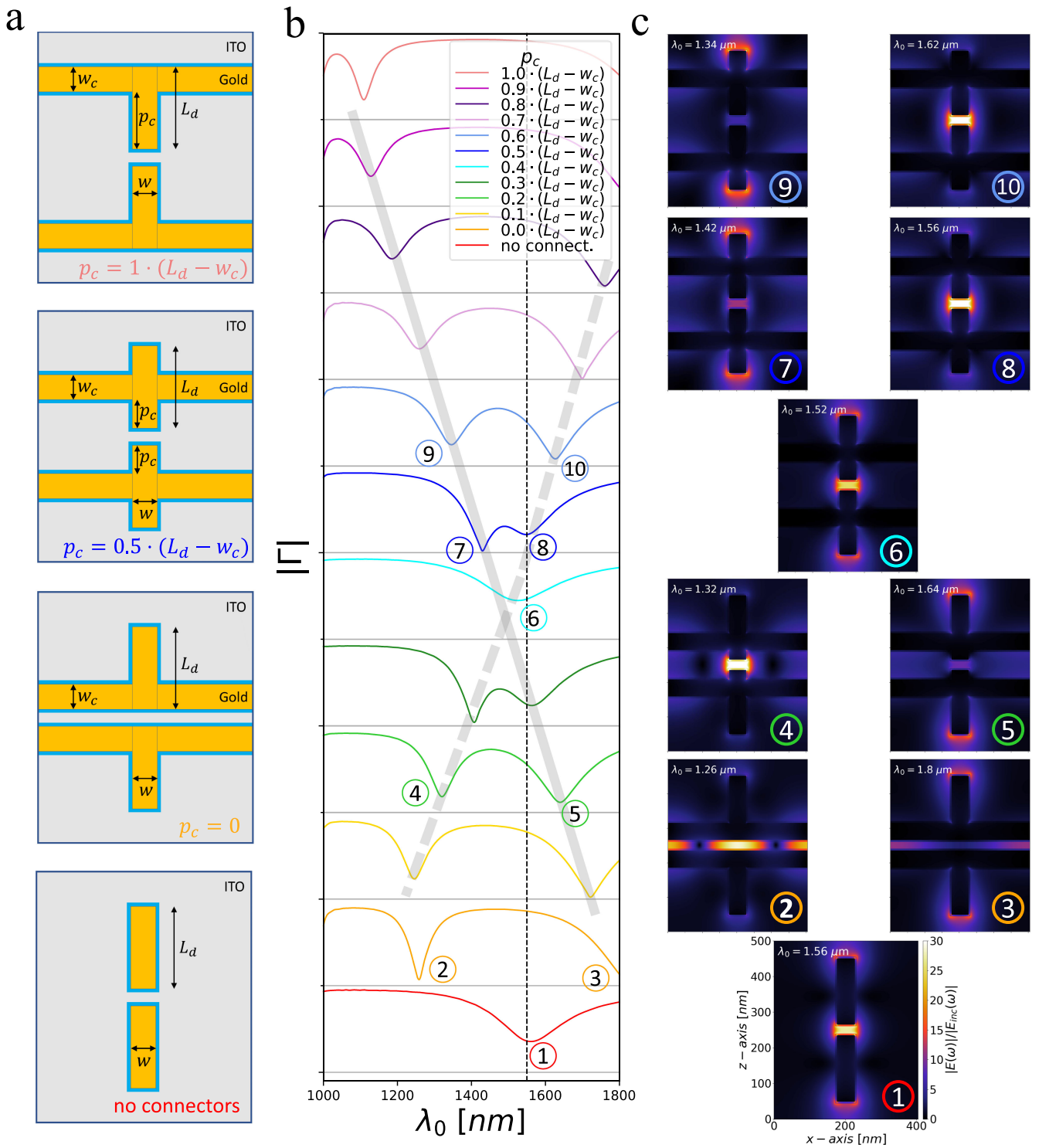

Fig. 7. Effect of the connector position for the pixel optimized in Fig. 6 ($g = 30$ nm, $L_d = 186$ nm, $a_x = 404$ nm, $t_m = 100$ nm): (a) illustration of different connector configurations, (b) reflection coefficient for varying connector positions as sketched in Fig. 7(a) – $|\Gamma|$ varies between 0 and 1 for all curves as marked by the grid lines, (c) field distribution for some resonances highlighted in Fig. 7(b).

secondary resonance with field enhancement at the extremities of the dipole nanoantenna. The average magnitude of reflection coefficient is lower (~ 0.2), as is the phase range ($\sim 244°$). The lower phase range is due to the fact λ_{ENZ} crosses $\lambda_c^{(2)}$ at higher voltages than it does for λ_c such that the phase shifting mechanism described in Section II-C is not fully exploited. We would need to further increase V_g (*i.e.*, N_{pert}) to extend the phase range.

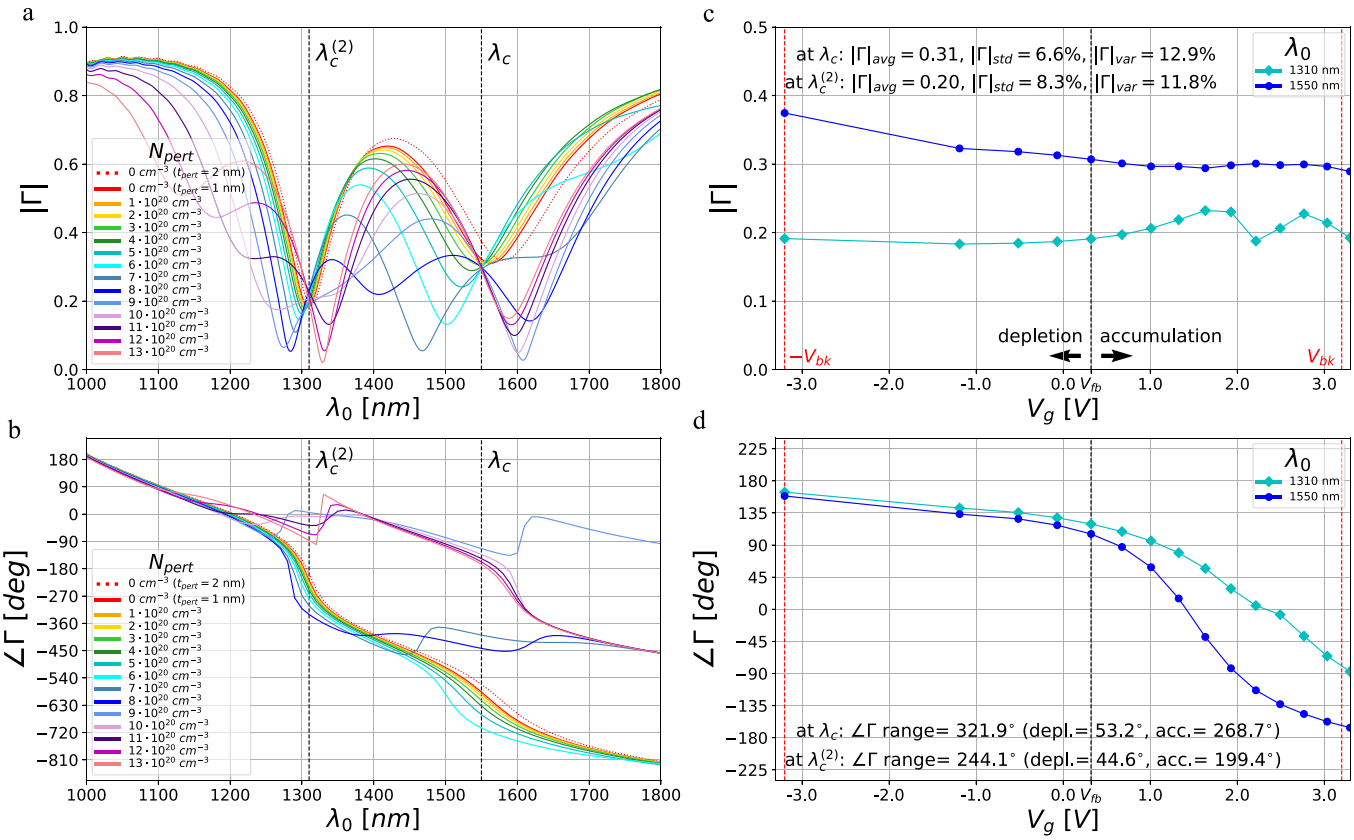

Fig. 8. Fourth optimized pixel with parameters with $g = 20$ nm, $L_d = 168$ nm, $a_x = 348$ nm, $t_m = 100$ nm, and $p_c = 0.5 \cdot (L_d - w_c)$: (a) $|\Gamma|$ and (b) $\angle\Gamma$ *vs.* λ_0 for varying N_{pert} within the t_{pert} layer. (c) $|\Gamma|$ and (d) $\angle\Gamma$ *vs.* V_g for λ_0 near λ_c. The phase plots are unwrapped for clarity.

F. Electrostatic Simulations

In this subsection, we use electrostatic modelling to justify the choice of the perturbation parameters N_{pert} and t_{pert} used to simulate in the previous subsections the optical response of our pixels due to voltage biasing. We first consider a 1D cross-sectional model of our MOS capacitor, and then we present a 2D model which takes into account corner configurations which can be found in nanostructures.

1) Simulation Details: The electrostatic modelling was conducted using Lumerical DEVICE, which solves the Poisson and drift-diffusion equations self-consistently [49]. We assume a work function for gold of $\phi_m = 5.1$ eV. For the oxide, we consider HfO_2, which is a high dielectric constant material of static relative permittivity $\varepsilon_{DC}^{(HfO_2)} = 25$ [50], [51]. ITO is treated as an n-doped semiconductor with $\varepsilon_{DC}^{(ITO)} = 9.3$, electron affinity $\chi_s = 4.8$ eV, band gap energy $E_g = 2.8$ eV, effective mass of electrons as in optical simulation ($m_n^* = 0.35 \cdot m_e$), and effective mass of holes $m_p^* = m_e$ [32]. Since E_g is large, the intrinsic carrier concentration n_i is very small. We assume an unperturbed carrier (electron) density in ITO of $N_0 = 3 \cdot 10^{20}$ cm^{-3} [32], which corresponds to a Fermi energy located within the conduction band, so that ITO behaves as a degenerate semiconductor. We consider ITO at a potential of $V_s = 0$ V (grounded) and we apply a gate voltage V_g to the metal as depicted in Fig. 9(a).

Breakdown fields for oxides used in MOS systems depend strongly on the deposition process. Assuming a breakdown field for HfO_2 of $E_{bk} = 6.4$ MV/cm [27], for a nominal thickness of $t_{ox} = 5$ nm, we obtain a breakdown voltage of $V_{bk} = 3.2$ V. The parameters of HfO_2 are similar to those of HAOL, *i.e.*, a nanolaminate comprised of layers of Al_2O_3 and HfO_2 ($\varepsilon_{DC}^{(HAOL)} = 22$ and $E_{bk} = 7.2$ MV/cm [32]), which could also be used in our phase shifting pixel as the insulating layer.

2) 1D Cross-Section Model: In Fig. 9(b), we show the potential V across the structure (oxide+ITO) for varying V_g, which reveals a flat band voltage $V_{fb} = 0.32$ V (value of V_g at which $V(y) = 0$). This means that for $V_g > V_{fb}$ the ITO layer goes into accumulation, whereas for $V_g < V_{fb}$ we have depletion.

From Fig. 9(c), we note that the carrier density in ITO increases with increasing gate voltage V_g. In order to maximize this carrier perturbation, we need to use an oxide with a high product of $\varepsilon_{DC} \cdot E_{bk}$. When no voltage is applied ($V_g = 0$ V), the MOS capacitor is slightly in depletion; we need to apply $V_g = V_{fb}$ in order to have an unperturbed carrier density across ITO, *i.e.*, $N_{pert} = N_0$ within the t_{pert} layer.

In Fig. 9(d) and (e), respectively, we show the complex permittivity ε_{Re} and ε_{Im} (at $\lambda_c = 1550$ nm, *i.e.*, the wavelength at which our pixels were optimized) by varying V_g and then N_{pert} within the perturbed ITO layer. We observe that for increasing V_g, ε_{Re} decreases becoming negative, and ε_{Im} increases, *i.e.*, the perturbed ITO layer becomes more and more metallic. Fig. 9(c) also shows that the perturbation of the carrier density is localized within a thickness of $\sim 1 - 2$ nm. In order to accurately resolve this perturbation, electrostatic computations were conducted

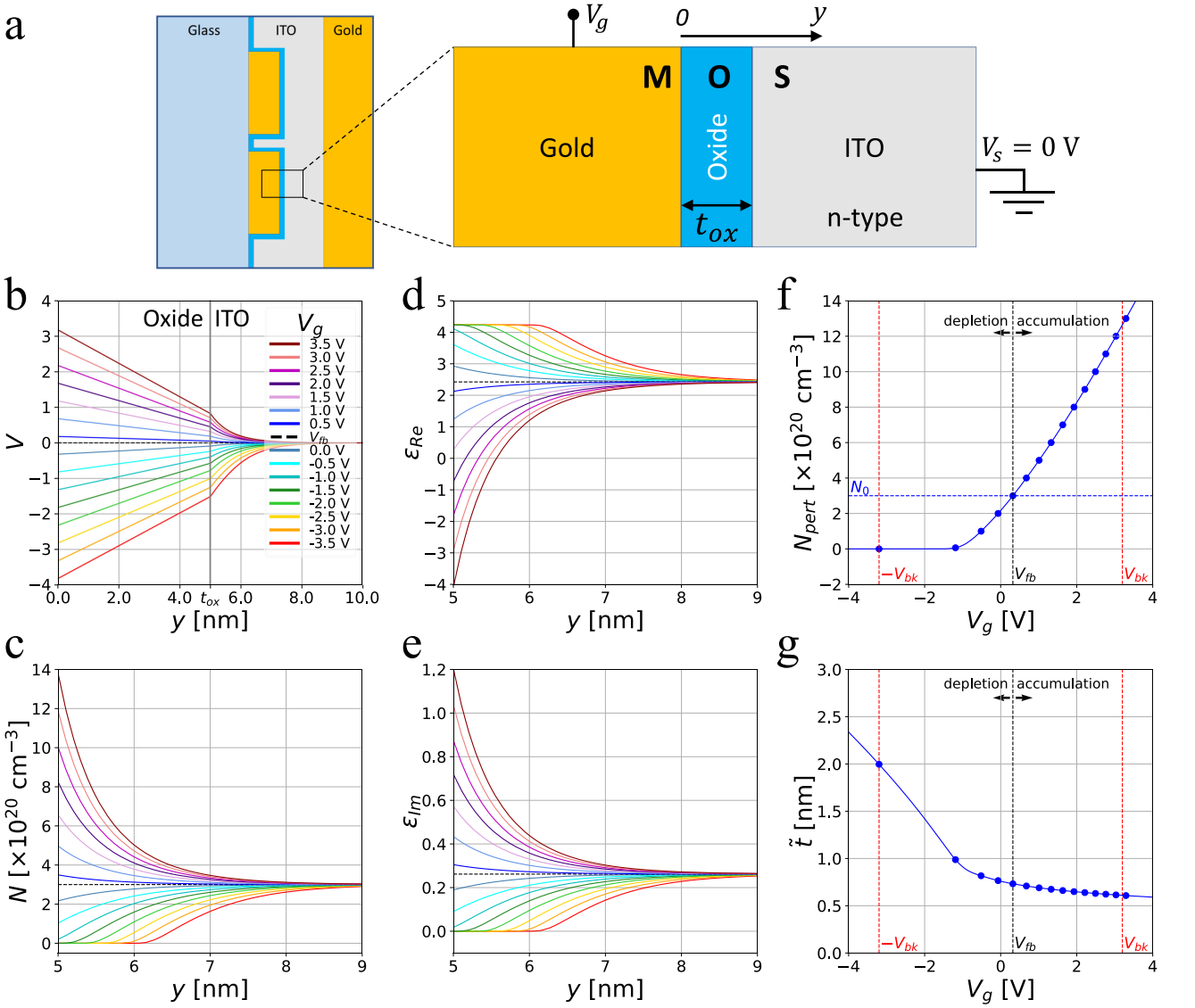

Fig. 9. (a) Side view of the plasmonic pixel and zoom of the MOS 1D cross-section modelled. (b) Voltage across the oxide and ITO for varying V_g. (c) Carrier density across ITO for varying V_g. (d), (e) ε_{Re} and ε_{Im} across ITO at λ_c for varying V_g. (f) N_{pert} as a function of V_g. (g) Effective perturbed ITO thickness $\tilde{t}$ as a function of V_g. Figs. 9(b)–(e) share the same legend.

with a discretization of ~ 0.05 nm, but this space step is challenging to apply in the corresponding 3D optical simulations, which are carried out here using a discretized space step of 1 nm. To model the perturbed carrier density in optical simulations, we need to homogenize the perturbation of the carrier density in ITO with respect to the unperturbed level N_0. This is done by considering the $N(y)$ curves in Fig. 9(c), and by identifying a constant carrier density $\tilde{N}$ and a constant thickness $\tilde{t}$ such that

$$\tilde{N} \cdot \tilde{t} = \int_{t_{ox}}^{+\infty} (N(y) - N_0) dy. \tag{1}$$

We set $\tilde{N} = \lim_{y \to t_{ox}^+} N(y) - N_0$, that is, we use the limit value that $N(y)$ reaches at the boundary between the oxide and ITO. Finally, we retrieve $N_{pert} = \tilde{N} + N_0$, as plotted in Fig. 9(f) for varying V_g within the breakdown voltage range (identified by vertical red dashed lines). We note that N_{pert} varies between 0 (depletion regime) and $\sim 13 \cdot 10^{20}$ cm^{-3} (accumulation regime) as used in the optical simulations. Inverting Eq. (1), we derive $\tilde{t}$, which is shown in Fig. 9(g) as a function of V_g. In accumulation, we obtain a nearly constant $\tilde{t}$ slightly lower than 1 nm, that we approximate with a perturbed ITO layer $t_{pert} = 1$ nm in the optical simulations. In depletion, the value of $\tilde{t}$ increases up to ~ 2 nm with decreasing V_g. The case of full depletion with $t_{pert} = 2$ nm was exploited in the optical simulations to further extend the phase range of the pixel. The blue dots in Fig. 9(f) and (g) correspond to the blue dots in the optical simulation results for the four optimized pixels reported in Figs. 3, 5, 6, and 8.

As the $t_{pert} = 1$ nm approximation in the accumulation regime may overestimate the pixel performance, we performed optical simulations where the thickness of the perturbed layer was taken to be $t_{pert} = 0.5$ nm, and the simulation domain was discretized with a space step of 0.5 nm. In this case, by re-optimizing the pixel to find a constant amplitude point at λ_c,

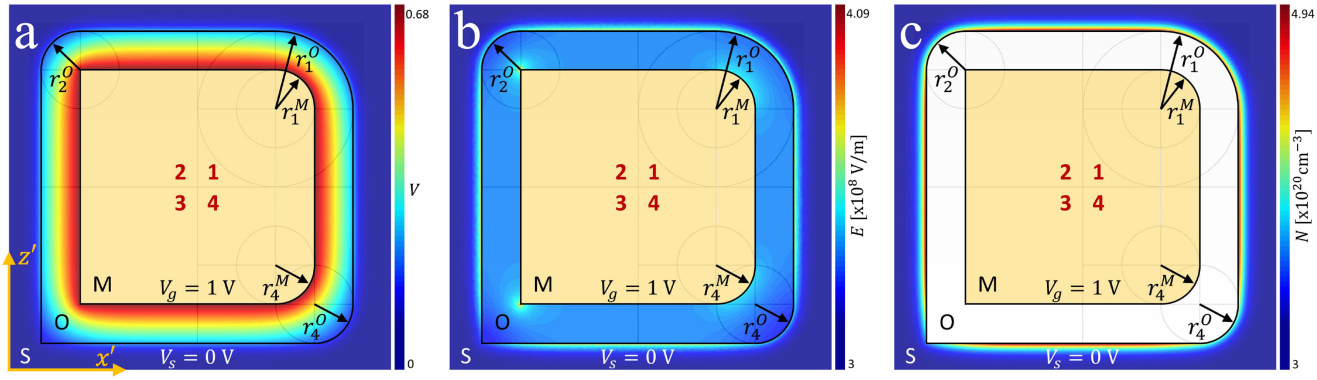

Fig. 10. (a) Potential, (b) electric field, and (c) carrier density distributions from electrostatic simulation of a representative MOS structure with four types of rounded corners for $V_g = 1$ V.

we obtained a lower magnitude of the reflection coefficient and an increased phase range.

3) 2D Correction to 1D Model: The MOS structure analyzed in 1D in Fig. 9 does not take into account the geometry of a nanoantenna. Since our plasmonic pixel (Fig. 1) is more complex as corners are involved, we performed a MOS study for a 2D geometry containing four different corner types as shown in Fig 10. In quadrant 1 (top right), we consider a rounded metal corner of radius $r_1^M = 5$ nm and a rounded oxide corner of radius $r_1^O = r_1^M + t_{ox} = 10$ nm. In quadrant 2 (top left), we have a square metal corner and a rounded oxide corner with $r_2^O = 5$ nm. In quadrant 3 (bottom left), both metal and oxide corners are square. In quadrant 4, both metal and oxide corners are rounded and of the same radius $r_4^M = r_4^O = 5$ nm. Fig. 10(a)–(c) show, respectively, the potential distribution $V(x,' z')$, the electric field distribution $|E(x,' z')|$ and the carrier density distribution $N(x,' z')$ for $V_g = 1$ V and ITO grounded ($V_s = 0$ V). We observe that V, E, and N exhibit a different behaviour at the corners compared to regions away from the corners where the behaviour of the 1D system is recovered. As the corner becomes more rounded (quadrant 1 in Fig. 10(c)), the carrier density N approaches that calculated for the 1D system. These results suggest that the perturbed layer in ITO should be modelled by a variable thickness depending on the roundness of the corners. However, the results of optical simulations of a nanoantenna with corners as in quadrant 1 (not shown), reproduce the physical operation of pixels containing all square corners with uniform t_{pert}; thus, for ease of simulation, square corners and uniform t_{pert} only are used throughout this paper. To consider round corners, the pixels as presented here would need to be re-optimized, as round corners produce a blue shift in the optical response due to the smaller total volume of rounded nanostructures versus square ones, all other geometrical parameters being equal.

III. Simulation of Phased Arrays for 1D Beam Steering

In Section II, we designed our pixels such that the pitch is small enough to avoid grating lobes due to the pitch size ($a_z, a_x < \lambda/2$) for any steering angle, yet large enough to avoid coupling between adjacent pixels due to near-field interaction. In order to validate our pixel designs for beam steering, we numerically test one of them (third optimized pixel in Fig. 6) in an array configuration. While in Section II we optimized the response of our pixels by applying periodic boundary conditions, which is equivalent to simulating an infinite array of pixels under the same perturbation, here, we create an array of pixels in the xz-plane, as sketched in Fig. 11(a). The arrangement of connectors makes the system controllable row by row (rows of pixels are identified by integers $q, q+1, \ldots$), which means that all nanoantennas in the same row will share the same potential, and thus the same phase of the reflection coefficient. By varying the phase associated with the pixels along z, we produce beam steering in the yz-plane ($\phi_s = 90°$) with a steering angle θ_s; in our example there is no steering in the xy-plane ($\phi_s = 0°$).

We cannot simulate arbitrarily large arrays with our FDTD model, so we apply periodic boundary conditions on an extended unit cell, that is formed by one pixel along x and M_z pixels along z. Thus, along z, each pixel produces a different phase of the reflection coefficient $\psi(q)$, with the position of the pixels in z labelled by $q = 1, \ldots, M_z$. To enforce a phase gradient along z in the array, which is necessary for beam steering, we need a constant phase difference between adjacent pixels along z, $\Delta\psi_z = \psi(q+1) - \psi(q)$. This sets a condition on $\Delta\psi_z$ in our simulations, which can only assume the values $|\Delta\psi_z| = 2\pi/M_z$. Knowing $\Delta\psi_z$, the steering angle θ_s can be analytically determined via the generalized form of Snell's law of reflection [52]:

$$k \sin\theta_s = \frac{\Delta\psi_z}{a_z} + k \sin\theta_i, \tag{2}$$

where $k = 2\pi n_{SiO_2}/\lambda_c$, θ_i is the angle of incidence (in our case, we have normal incidence, *i.e.*, $\theta_i = 0$) and θ_s is the angle of the reflected/steered beam.

We consider an extended unit cell with $M_z = 8$ and $\Delta\psi_z = -45°$. The array is excited by a monochromatic plane wave at λ_c which is z-polarized and normally incident on the metasurface. In Fig. 11(b), we plot the phase of the reflected field E_z. The reflected field is obtained by subtracting the incident field from the total field – a dashed white line in Fig. 11(b) separates the FDTD scattered-field (SF) and total-field (TF) regions, and in the TF region we see the $M_z = 8$ pixels of the extended unit cell

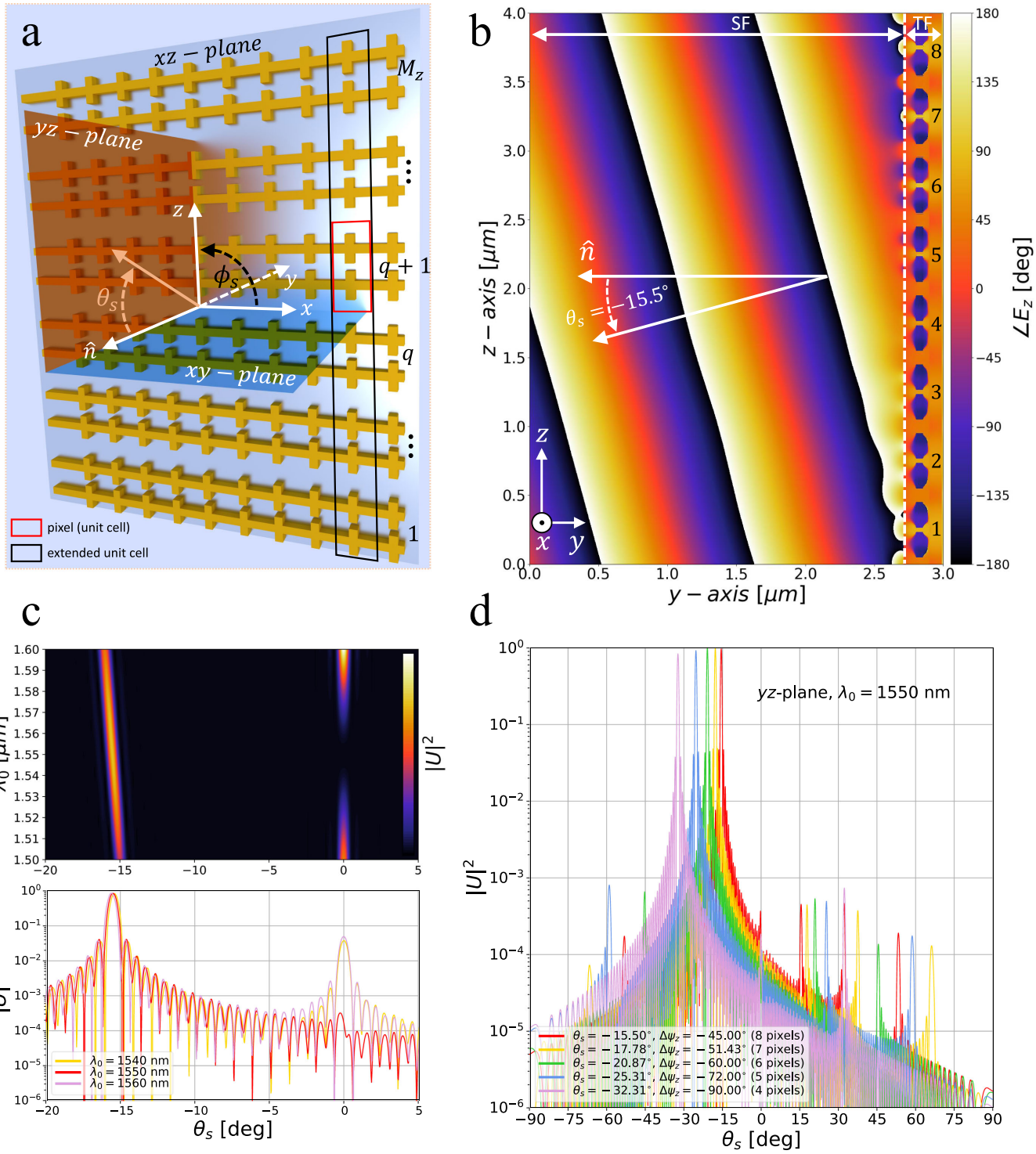

Fig. 11. (a) Sketch of an array of pixels with coordinates, (b) $\angle E_z$ and (c) radiation pattern in the yz-plane ($\phi_s = 90°$) for an extended unit cell ($M_z = 8$, $\theta_s = -15.5°$), (d) radiation pattern for extended unit cells with $M_z = 4, 5, 6, 7, 8$ pixels.

aligned along z. We determine the voltage that must be applied to each row to produce the required phase of the reflection coefficient $\psi(q)$ across the extended unit cell by using the curve for $\lambda_c = 1550$ nm in Fig. 6(d) (which depends on Fig. 9(f)). The voltages that must be applied to the 8 pixels in Fig. 11(b) are $V_g^{(q)} = \{-3, 0.169, 0.908, 1.23, 1.465, 1.694, 2.025, 2.737\}$ V for $q = 1, \ldots, 8$. In Fig. 11(b), we note that the phase front of the reflected wave is flat and propagates at an angle of $\theta_s = -15.5°$ with respect to the normal to the plane of the array, as confirmed by Eq. (2). We also find that the amplitude of the

reflected field E_z is nearly uniform with a percentage variation $|E_z|_{var} = 5.6\%$. These phase and amplitude profiles indicate beam steering.

The flat phase front reflected from the array only provides qualitative information about the steering. To further validate the beam steering, the radiation pattern in the far-field must be observed. From the near-fields in the reflection region, we calculate the far-fields via a near-to-far-field transformation [44], and then obtain the radiation pattern by squaring the far-fields. This near-to-far-field transformation is carried out considering $P_z = 25$ periods of the extended unit cell such to mimic an array with 200 pixels. The radiation pattern allows us to quantify how the electromagnetic power is distributed in space as a function of angle, and thus, to quantify the quality of the beam steering in terms of intensity of the long-period grating lobes. In Fig. 11(c), we show the normalized radiation pattern $|U(\theta_s, \phi_s)|^2$ in the yz-plane ($\phi_s = 90°$). In the top panel we show the contour plot of the far-field reflected power as a function of wavelength (varying from $\lambda_0 = 1500$ nm to 1600 nm) and far-field angle θ_s. The contour plot reveals that near λ_c the specular reflection in the normal direction disappears (black region in the colour band for $\theta_s = 0°$). Looking at this black region, we calculate the wavelength range such that the far-field intensity in the normal direction is two orders of magnitude lower than the main beam, which yields an optical bandwidth for beam steering, in this case of ~ 10 nm. The bottom panel contains three curves extracted from the contour plot on a log scale, where we see that for $\lambda_c = 1550$ nm the long-period grating lobe at $\theta_s = 0°$ is more than two orders of magnitude less intense than for $\lambda_0 = 1540$ and 1560 nm. These results validate the optimization at λ_c of the single pixel, as they show that at λ_c the specular reflection is negligible and the beam is completely steered.

In Fig. 11(d), we show the radiation patterns for different values of $M_z = \{4, 5, 6, 7, 8\}$, calculated via near-to-far-field transformation using $P_z = \{50, 40, 34, 29, 25\}$, respectively, such that $M_z \cdot P_z \sim 200$. These M_z values correspond to decreasing values of $\Delta\psi_z$ and thus steering angle θ_s, as reported in the legend of Fig. 11(d). From phased antenna array theory, we know that the radiation pattern of the array is obtained by multiplying the radiation pattern of the single emitter F with an array factor A that depends on the arrangement of the emitters, *i.e.*, $|U(\theta_s, \phi_s)|^2 = |F(\theta_s, \phi_s)|^2 |A(\theta_s, \phi_s)|^2$. As $A(\theta_s, \phi_s)$ reaches the same maximum value for any steering angle, the fact that the peak of the radiation patterns in Fig. 11(d) decreases with increasing steering angle suggests that each nanoantenna exhibits a dipole-like radiation pattern in reflectance. All the radiation patterns show long-period grating lobes which are more than three orders of magnitude lower than the main lobe, confirming beam steering over a wide angular range. We note that this array simulation approach does not take into account the limited phase range of the pixel, as M_z is chosen such that $(M_z - 1)|\Delta\psi_z|$ is lower than the phase range of the pixel. The long-period grating lobes that we observe are only due to the non-uniform amplitude of the reflection coefficient as V_g varies, and they obey the diffraction grating equation:

$$\sin\theta_s^{(m)} = m\lambda/(a_z M_z), \tag{3}$$

where $a_z M_z$ is the size of the extended unit cell (our long period), and m is the diffraction order ($m = 1$ identifies the main lobe). Supplementary Movies 1 and 2 show the time-domain evolution of the absolute value of the electric field for $M_z = 8$ ($\Delta\psi_z = -45°, \theta_s = -15.5°$) and $M_z = 4$ ($\Delta\psi_z = -90°, \theta_s = -32.31°$). The scattered-field region contains only the steered beam and is thus made large in the simulation for visual clarity, while the total-field region contains both the reflected and incident fields, and is thus limited to the vicinity of the metasurface where the input signal is injected. As this is a time-domain simulation, we find that the steering does not occur instantaneously, as the phase gradient responsible for the creation of the steered beam takes ~ 80 fs to build up due to plasmonic resonance delays across the extended unit cell.

IV. Conclusion

We propose a novel plasmonic pixel for beam steering applications in reflectarray configurations. The pixel is of subwavelength dimensions, and exhibits a reflection coefficient that, at a specific operating wavelength, varies with applied voltage over a large phase range with nearly constant amplitude. The structure consists of a plasmonic dipole nanoantenna on a substrate covered conformally by a thin oxide layer, which is then covered by ITO and a gold backplane. Electrically, the structure forms a MOS capacitor with the nanoantenna acting as the electrical contact of the capacitor. The MOS capacitor is exploited to perturb the free electron density within a region of ITO in contact with the oxide. This perturbed layer of ITO will experience a change of its epsilon-near-zero wavelength as a function of applied voltage, eventually crossing the resonance wavelength of the nanoantenna. When this occurs, the environment surrounding the nanoantenna switches from all dielectric to one containing a metallic shell. This abruptly changes the resonance of the nanoantenna and causes a large phase shift in its reflection coefficient.

We found that the phase range of the reflection coefficient depends on the maximum carrier density perturbation induced in ITO which is bounded by the oxide breakdown voltage. Moreover, the magnitude of the reflection coefficient at the operating wavelength depends on the thickness of this perturbation, but can be made uniform across the phase range by optimizing the geometrical parameters. We analyzed the performance of several pixel designs and found that a phase range of 330° is possible with a nearly flat magnitude of the reflection coefficient of 0.2; higher magnitudes of ~ 0.4 are possible if we can accept a phase range of 300°. The reflection coefficient amplitude can be improved by using materials with lower losses, and this is currently under investigation.

We also found that there is an optimal position for the electrical connectors where they contribute minimally to the optical response of the nanoantenna. However, in an alternate position, their effect may be exploited for realizing dual-band beam steering. Though the performance of the proposed pixel is primarily limited by the breakdown field of the oxide, the phase and amplitude responses of the reflection coefficient achieved with materials currently available are highly promising for beam

steering applications, as demonstrated by our 3D optical simulations of beam steering in 1D.

ACKNOWLEDGMENT

We acknowledge computational support from SciNet and Compute Canada, and financial support from NSERC and Huawei Technologies Canada.

REFERENCES

[1] M. J. Heck, "Highly integrated optical phased arrays: Photonic integrated circuits for optical beam shaping and beam steering," *Nanophotonics*, vol. 6, pp. 93–107, 2017.
[2] N. Meinzer, W. L. Barnes, and I. R. Hooper, "Plasmonic meta-atoms and metasurfaces," *Nature Photon.*, vol. 8, pp. 889–898, 2014.
[3] P. Genevet, F. Capasso, F. Aieta, M. Khorasaninejad, and R. Devlin, "Recent advances in planar optics: From plasmonic to dielectric metasurfaces," *Optica*, vol. 4, pp. 139–152, 2017.
[4] J. Scheuer, "Metasurfaces-based holography and beam shaping: Engineering the phase profile of light," *Nanophotonics*, vol. 6, pp. 137–152, 2017.
[5] S. Chen, Z. Li, Y. Zhang, H. Cheng, and J. Tian, "Phase manipulation of electromagnetic waves with metasurfaces and its applications in nanophotonics," *Adv. Opt. Mater.*, vol. 6, 2018, Art. no. 1800104.
[6] M. Papaioannou, E. Plum, E. T. Rogers, and N. I. Zheludev, "All-optical dynamic focusing of light via coherent absorption in a plasmonic metasurface," *Light: Sci. Appl.*, vol. 7, 2018, Art. no. 17157.
[7] W. T. Chen *et al.*, "A broadband achromatic metalens for focusing and imaging in the visible," *Nature Nanotechnol.*, vol. 13, pp. 220–226, 2018.
[8] P. Arroyo Huidobro, S. A. Maier, and J. B. Pendry, "Tunable plasmonic metasurface for perfect absorption," *EPJ Appl. Metamaterials*, vol. 4, 2017, Art. no. 6.
[9] T. Lee, J. Jang, H. Jeong, and J. Rho, "Plasmonic- and dielectric-based structural coloring: From fundamentals to practical applications," *Nano Convergence*, vol. 5, 2018, Art. no. 1.
[10] A. Silva *et al.*, "Performing mathematical operations with metamaterials," *Science*, vol. 343, pp. 160–163, 2014.
[11] L. Huang, S. Zhang, and T. Zentgraf, "Metasurface holography: From fundamentals to applications," *Nanophotonics*, vol. 7, pp. 1169–1190, 2018.
[12] A. Calà Lesina, L. Ramunno, and P. Berini, "Dual-polarization plasmonic metasurface for nonlinear optics," *Opt. Lett.*, vol. 40, pp. 2874–2877, 2015.
[13] F. Yue *et al.*, "Vector vortex beam generation with a single plasmonic metasurface," *ACS Photon.*, vol. 3, pp. 1558–1563, 2016.
[14] A. Calà Lesina, P. Berini, and L. Ramunno, "Vectorial control of nonlinear emission via chiral butterfly nanoantennas: Generation of pure high order nonlinear vortex beams," *Opt. Express*, vol. 25, pp. 2569–2582, 2017.
[15] S. Zeng *et al.*, "Graphene-gold metasurface architectures for ultrasensitive plasmonic biosensing," *Adv. Mater.*, vol. 27, pp. 6163–6169, 2015.
[16] N. Jiang, X. Zhuo, and J. Wang, "Active plasmonics: Principles, structures, and applications," *Chem. Rev.*, vol. 118, pp. 3054–3099, 2018.
[17] L. Kang, R. P. Jenkins, and D. H. Werner, "Recent progress in active optical metasurfaces," *Adv. Opt. Mater.*, vol. 7, 2019, Art. no. 1801813.
[18] A. M. Shaltout, V. M. Shalaev, and M. L. Brongersma, "Spatiotemporal light control with active metasurfaces," *Science*, vol. 364, 2019, Art. no. eaat3100.
[19] J. Li *et al.*, "Addressable metasurfaces for dynamic holography and optical information encryption," *Sci. Advances*, vol. 4, 2018, Art. no. eaar6768.
[20] L. Zhang *et al.*, "Space-time-coding digital metasurfaces," *Nature Commun.*, vol. 9, 2018, Art. no. 4334.
[21] X. Yin *et al.*, "Active chiral plasmonics," *Nano Lett.*, vol. 15, pp. 4255–4260, 2015.
[22] X. Duan, S. Kamin, and N. Liu, "Dynamic plasmonic colour display," *Nature Commun.*, vol. 8, 2017, Art. no. 14606.
[23] B. Ratni, A. de Lustrac, G.-P. Piau, and S. N. Burokur, "Electronic control of linear-to-circular polarization conversion using a reconfigurable metasurface," *Appl. Phys. Lett.*, vol. 111, 2017, Art. no. 214101.
[24] Z. Wang *et al.*, "Metasurface-based focus-tunable mirror," *Opt. Express*, vol. 27, pp. 30332–30339, 2019.
[25] S. Busschaert *et al.*, "Beam steering with a nonlinear optical phased array antenna," *Nano Lett.*, vol. 19, pp. 6097–6103, 2019.
[26] A. Forouzmand, M. M. Salary, S. Inampudi, and H. Mosallaei, "A tunable multigate indium-tin-oxide-assisted all-dielectric metasurface," *Adv. Opt. Mater.*, vol. 6, 2018, Art. no. 1701275.
[27] A. Olivieri *et al.*, "Plasmonic nanostructured metal-oxide-semiconductor reflection modulators," *Nano Lett.*, vol. 15, pp. 2304–2311, 2015.
[28] Z. Zhu, P. G. Evans, R. F. Haglund, and J. G. Valentine, "Dynamically reconfigurable metadevice employing nanostructured phase-change materials," *Nano Lett.*, vol. 17, pp. 4881–4885, 2017.
[29] A. Komar *et al.*, "Dynamic beam switching by liquid crystal tunable dielectric metasurfaces," *ACS Photon.*, vol. 5, pp. 1742–1748, 2018.
[30] M. C. Sherrott *et al.*, "Experimental demonstration of $>230^\circ$ phase modulation in gate-tunable graphene-gold reconfigurable mid-infrared metasurfaces," *Nano Lett.*, vol. 17, pp. 3027–3034, 2017.
[31] Y.-W. Huang *et al.*, "Gate-tunable conducting oxide metasurfaces," *Nano Lett.*, vol. 16, pp. 5319–5325, 2016.
[32] G. K. Shirmanesh, R. Sokhoyan, R. A. Pala, and H. A. Atwater, "Dual-gated active metasurface at 1550 nm with wide ($>300^\circ$) phase tunability," *Nano Lett.*, vol. 18, pp. 2957–2963, 2018.
[33] J. Sun, E. Timurdogan, A. Yaacobi, E. S. Hosseini, and M. R. Watts, "Large-scale nanophotonic phased array," *Nature*, vol. 493, pp. 195–199, 2013.
[34] M. Xun *et al.*, "Phase tuning in two-dimensional coherently coupled vertical-cavity surface-emitting laser array," *Appl. Opt.*, vol. 55, pp. 5439–5443, 2016.
[35] J. Lee *et al.*, "Ultrafast electrically tunable polaritonic metasurfaces," *Adv. Opt. Mater.*, vol. 2, pp. 1057–1063, 2014.
[36] E. Feigenbaum, K. Diest, and H. A. Atwater, "Unity-order index change in transparent conducting oxides at visible frequencies," *Nano Lett.*, vol. 10, pp. 2111–2116, 2010.
[37] H. W. Lee *et al.*, "Nanoscale conducting Oxide PlasMOStor," *Nano Lett.*, vol. 14, pp. 6463–6468, 2014.
[38] A. Forouzmand and H. Mosallaei, "Real-time controllable and multi-functional metasurfaces utilizing indium tin oxide materials: A phased array perspective," *IEEE Trans. Nanotechnol.*, vol. 16, no. 2, pp. 296–306, Mar. 2017.
[39] M. Alavirad, A. Olivieri, L. Roy, and P. Berini, "Fabrication of electrically contacted plasmonic Schottky nanoantennas on silicon," *Chin. Opt. Lett.*, vol. 16, 2018, Art. no. 050007.
[40] C. Hahn, A. Hajebifard, and P. Berini, "Helium focused ion beam direct milling of plasmonic heptamer-arranged nanohole arrays," *Nanophotonics*, vol. 9, pp. 393–399, 2020.
[41] J.-M. Guay *et al.*, "Laser-written colours on silver: Optical effect of alumina coating," *Nanophotonics*, vol. 8, pp. 807–822, 2019.
[42] X. Deng *et al.*, "Single-Order, subwavelength resonant nanograting as a uniformly hot substrate for surface-enhanced raman spectroscopy," *Nano Lett.*, vol. 10, pp. 1780–1786, 2010.
[43] [Online]. Available: URL https://www.asml.com/en/technology, 2019.
[44] A. Taflove and S. C. Hagness, *Computational Electrodynamics: The Finite-Difference Time-Domain Method*. 3rd Ed. Norwood, MA, USA: Artech House, 2005.
[45] A. Calà Lesina, A. Vaccari, P. Berini, and L. Ramunno, "On the convergence and accuracy of the FDTD method for nanoplasmonics," *Opt. Express*, vol. 23, 2015, Art. no. 10481.
[46] K. M. McPeak *et al.*, "Plasmonic films can easily be better: Rules and recipes," *ACS Photon.*, vol. 2, pp. 326–333, 2015.
[47] D. L. Wood, K. Nassau, T. Y. Kometani, and D. L. Nash, "Optical properties of cubic hafnia stabilized with yttria," *Appl. Opt.*, vol. 29, pp. 604–607, 1990.
[48] C. A. Riedel, K. Sun, O. L. Muskens, and C. de Groot, "Nanoscale modeling of electro-plasmonic tunable devices for modulators and metasurfaces," *Opt. Express*, vol. 25, 2017, Art. no. 10031.
[49] [Online]. Available: URL https://www.lumerical.com/, 2020.
[50] G. D. Wilk, R. M. Wallace, and J. M. Anthony, "High-κ gate dielectrics: Current status and materials properties considerations," *J. Appl. Phys.*, vol. 89, pp. 5243–5275, 2001.
[51] J. Robertson, "High dielectric constant gate oxides for metal oxide Si transistors," *Reports Progress Phys.*, vol. 69, pp. 327–396, 2006.
[52] N. Yu *et al.*, "Light propagation with phase discontinuities: Generalized laws of reflection and refraction," *Science*, vol. 334, pp. 333–337, 2011.

Antonino Calà Lesina received the B.Sc. degree in electronics engineering and the M.Sc. degree in telecommunications engineering from the University of Catania, Italy, in 2006 and 2009, respectively and the Ph.D. degree in information and communication technologies in 2013 from the University of Trento, Italy, conducting his research in computational electromagnetics at the Fondazione Bruno Kessler. He joined the University of Ottawa in 2013 as a Postdoctoral Fellow in the groups of professors Lora Ramunno and Pierre Berini, where he is a Research Associate since 2018. In 2020 he will join Leibniz University Hannover, Germany as a W2 Professor (tenure track). His research focuses on large-scale computational nanophotonics, optical design, and metamaterials.

Dominic Goodwill received the Ph.D. degree in nonlinear optics of III-V semiconductors from Heriot-Watt University, UK, in 1991. He is a Senior Principal Engineer at Huawei Canada, focused on communications and sensing applications of silicon photonics. Previously, he developed and deployed video network software products at GENBAND Corporation, developed VCSEL and DFB optical interconnect technology and MEMS switching at Nortel, and polymer and free-space photonics at University of Colorado. His professional contributions include program subcommittee member / chair at Optical Fiber Communications conference 2017-2020, general and program chair of IEEE Optical Interconnects Conference 2015-2017, and fiber-optics chair of InfiniBand standard in 2000. He has 50 issued U.S. patents.

Eric Bernier is the team Leader for the Advanced Photonic Team at Huawei Canada. Eric is responsible for exploring and developing into products new and innovative photonic components for Huawei. His team is looking at: Optical network line components, Optical Interconnect, and Datacenter technologies. Prior to Huawei, Eric held the position of CTO (VP Technology) at the Canadian Advanced Network, and Senior Technology Advisor at Nortel Networks. Eric has a Masters Degree in Electrical Engineering from McGill University.

Lora Ramunno received the Ph.D. degree in physics from the University of Toronto in 2002. After a year in a high-tech start-up, she returned to academia as a postdoctoral fellow at uOttawa. Since 2007, she has been a faculty member in Physics at uOttawa where she is currently Full Professor. She held a Canada Research Chair in Computational Nanophotonics from 2007-2017, and was the recipient of an Early Researcher Award in 2007. Her theoretical/computational research focuses on nonlinear and nano-optics, including intense laser-matter interaction, nanophotonics, nonlinear optical microscopy and photonic devices. She also has several successful industrial collaborative projects. Prof. Ramunno is a fellow of the Max-Planck-UOttawa Centre for Extreme and Quantum Photonics, a fellow of the NRC-UOttawa Joint Centre for Extreme Photonics, and a member of the uOttawa Centre for Research in Photonics.

Pierre Berini received the Ph.D. and M.Sc.A. degrees in electrical engineering from École Polytechnique de Montréal, Canada, and the B.E.Sc. and B.Sc. degrees in electrical engineering and computer science, respectively, from the University of Western Ontario, Canada. Dr. Berini is Distinguished University Professor of Electrical Engineering and of Physics, University Research Chair in Surface Plasmon Photonics, and Director of the Centre for Research in Photonics at the University of Ottawa. He was the Founder and Chief Technology Officer of a venture capital financed company and he collaborates on an ongoing basis with industry. Dr. Berini has received an NSERC Steacie Fellowship, an NSERC Discovery Accelerator, a Premier of Ontario Research Excellence Award (PREA), the University of Ottawa Young Researcher of the Year Award, an URSI Young Scientist Award, a George S. Glinski Award for Excellence in Research, and is a Canada Foundation for Innovation researcher. Dr. Berini is a Fellow of the IEEE, a Fellow of the OSA, a Fellow of the Canadian Academy of Engineering, and a Fellow of the Royal Society of Canada. He has published 12 book chapters, approximately 500 scientific and technical papers in peer-reviewed periodicals and conference proceedings, and is an inventor or Co-Inventor on 23 patents ($h = 47$). He was an Associate Editor of Optics Express and a Managing Editor of Nanophotonics, and is presently an Associate Editor of Optica. He contributes on an ongoing basis to the organization of several international conferences in photonics. His research interests span many areas of optics and photonics, with surface plasmons and their applications being of particular current interest.